An electrochemical sensing platform based on liquid-liquid microinterface arrays formed in laser-ablated glass membranes

Eva Alvarez de Eulate,[a] Jorg Strutwolf,[b] Yang Liu,[a] Kane O'Donnell[c] and Damien W. M. Arrigan[a,*]

[a] Nanochemistry Research Institute, Department of Chemistry, Curtin University, GPO Box U1987, Perth, Western Australia, 6845, Australia.

[b] Department of Chemistry, Institute of Organic Chemistry, University of Tübingen, Germany.

[c] Department of Physics, Astronomy and Medical Radiation Science, Curtin University, GPO Box U1987, Perth, Western Australia, 6845, Australia.

* Email d.arrigan@curtin.edu.au, phone +61-(0)8-9266-9735.

Abstract

Arrays of microscale interfaces between two immiscible electrolyte solutions (µITIES) were formed using glass membranes perforated with microscale pores by laser ablation. Square arrays of 100 micropores in 130 µm thick borosilicate glass coverslips were functionalised with trichloro(1H,1H,2H,2H-perfluorooctyl)silane on one side, to render the surface hydrophobic and support the formation of aqueous-organic liquid-liquid micro-interfaces. The pores show a conical shape, with larger radii at the laser entry side (26.5 µm) than at the laser exit side (11.5 µm). The modified surfaces were characterised by contact angle measurements and x-ray photoelectron spectroscopy. The organic phase was placed on the hydrophobic side of the membrane, enabling the array of µITIES to be located at either the wider or narrower pore mouth. The electrochemical behaviour of the µITIES arrays were investigated by tetrapropylammonium ion transfer across water – 1,6-dichlorohexane interfaces together with finite element computational simulations. The data suggest that the smallest micro-interfaces (formed on the

laser exit side) were located at the mouth of the pore in hemispherical geometry, whilst the larger micro-interfaces (formed on the laser entry side) were flatter in shape but exhibited more instability due to the significant roughness of the glass around the pore mouths. The glass membrane-supported μITIES arrays presented here provide a new platform for chemical and biochemical sensing systems.

INTRODUCTION

Electrochemistry at liquid-liquid interfaces has shown its utility for the detection of an extensive variety of inorganic and organic species,[1-3] as well as provision of important information regarding the thermodynamics and kinetics of reactions at soft interfaces.[4] Miniaturisation of the interface between two immiscible electrolyte solutions (ITIES) improves the sensing capabilities of these liquid devices, as it increases the rate of mass transport and reduces the cell resistance. This also brings the advantages of reducing the amounts of reagents used and improved portability, which can aid development of point-of-care devices.[5]

Fabrication of micro- and nano- platforms to support liquid-liquid interfaces has enabled the expansion of the application of this technique. In the 1980s, Taylor and Girault introduced micrometer-sized ITIES supported at glass pipette tips (25 μm) to study ion transfer reactions.[6] Since then, new approaches to miniaturise soft interfaces via micro-pipettes and micro-holes have been reported with a variety of materials, geometries and fabrication processes. Regarding the fabrication of single micro- or nano-ITIES, the use of CO_2-laser-based glass pipette pullers[5,7] is the most common approach to produce glass micro and nano-tips,[7] although Stockmann et *al.* produced a 25 μm diameter glass pipette by acid (aqua regia) etching of Pt-wire inserted in a glass capillary.[8] At present, glass nano-pipettes are extensively used as probes for scanning electrochemical microscopy (SECM)[9,10] and scanning ion-conductance microscopy (SICM).[11,12] Various groups[13] [14] [15] have established the fabrication of nano-pipettes in quartz to elucidate the kinetics of ion transfer processes at the ITIES. Also, polymers such as polyethylene terephthalate (PET),[16] polyester[17,18] and polyimide[19,20] have been examined as membranes to locate micro-ITIES for

electrochemical analysis. For most of these polymer films, laser micromachining was used as the fabrication process although a single-hole in a polyvinylchloride film was also simply pierced with a sharp needle.[21] The first micro-hole array supported micro-ITIES was reported by Campbell and Girault,[16] who used a micromachined PET substrate consisting of 66 holes prepared by ablation with a UV excimer laser.[22] Recent studies have reported using such micro-hole array PET films for anion transfer at water – polyvinylchloride-gelled o-nitrophenyloctylether (W/PVC-NPOE) interfaces[23] and for facilitated proton transfer.[24,25] Similarly, studies of assisted ion transfers at polyimide-supported micro-ITIES examined the interface location as well as parameters such as micro-hole radius, membrane thickness and the method of electrolyte solution introduction.[19,26]

On the other hand, combinations of photolithography or electron beam lithography with chemical etching were used to fabricate micropore arrays in silicon[27] and nanopore arrays in silicon nitride (Si_3N_4),[28] respectively. Micropores with radii ranging from 6.5 to 26.6 µm in silicon of 100 µm thickness were used to form micro-ITIES,[27] while the nanopores in Si_3N_4 with radii in the range of 17 - 230 nm were used to form nano-ITIES.[28,29] Recently, the fabrication of nanopores to form nano-ITIES was extended to rapid prototyping by focused ion beam (FIB) milling in 50 nm thick Si_3N_4 (e.g. radii 30 – 80 nm).[25,30] Thus, glass pipettes together with polymer, silicon or silicon nitride membranes have been used to form micro/nano-ITIES and their arrays.

Surprisingly, there has been no report, to our knowledge, on glass membrane-based arrays as a platform for electrochemical sensing at liquid-liquid interfaces. The aim of this report is to present a glass membrane micropore array, consisting of 100 pores micro-drilled in 130 µm thick borosilicate glass substrates by laser ablation. The significance of this work lies in the simplicity of the fabrication, the well-known surface chemistry of glass, and the already wide use of glass in chemical sensing devices.


EXPERIMENTAL

Reagents. All reagents were purchased from Sigma Aldrich. 10 mM tetradodecylammonium tetrakis(4-

chlorophenyl)borate (TDA$^+$TPBCl$^-$) was prepared in water-saturated 1,6-dichlorohexane (DCH). An organic reference solution of 10 mM tetradodecylammonium chloride (TDACl) in 10 mM LiCl was prepared in DCH-saturated water. The aqueous background electrolyte was 10 mM lithium chloride solution prepared in DCH-saturated water. Stock solutions of tetrapropylammonium chloride (TPACl) were also prepared in the aqueous background electrolyte. Purified water with a resistivity of 18.2 MΩ cm (Milli-Q, Millipore Pty. Ltd., Australia) was used for preparation of aqueous solutions.
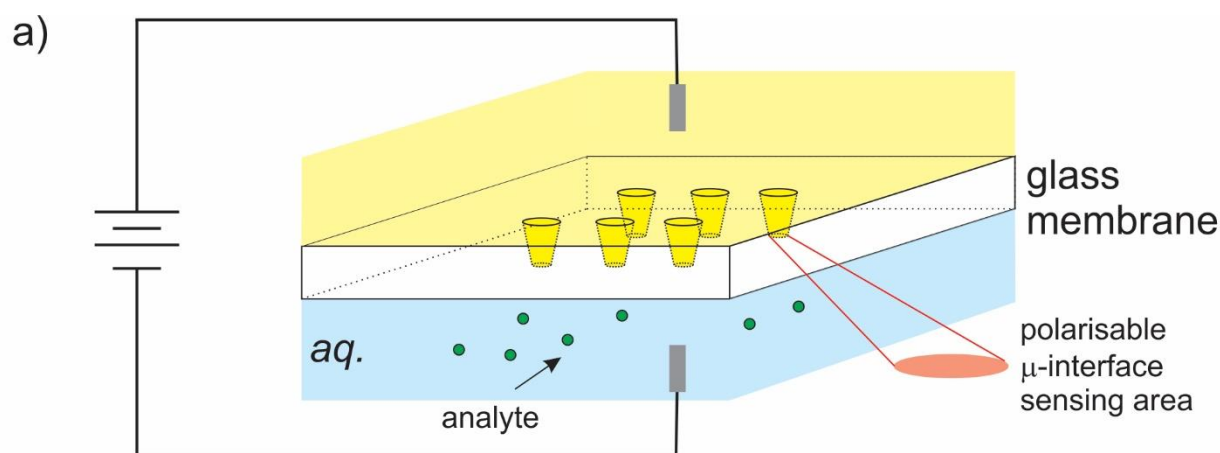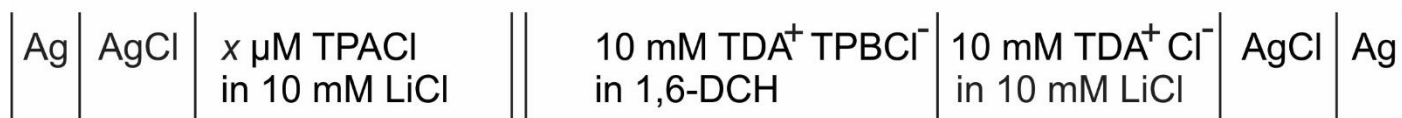
Scheme 1. a) Illustration of the glass micro-pore array and b) the electrochemical cell composition.

Glass membrane fabrication. The glass membranes were fabricated at the Australia National Fabrication Facility, at the South Australia Node (ANNF-SA, University of South Australia, Adelaide, South Australia) and at the Optofab Node (ANFF-OptoFab, Macquarie University, New South Wales). Micropore arrays in 10 x 10 square array format were drilled via laser ablation (at ANNF-Optofab) in a *ca.* 130 µm thick borosilicate substrate (13 mm diameter coverslips, type G402, Proscitech, Australia). The laser employed was a 4th harmonic, diode pumped Nd:YAG system, producing 266 nm (UV) light with 10 ns pulses, suitable for glass machining. The machining setup included a spinning wedge trepanning optic (4000 RPM) to rapidly drill circular holes through a f = 60 mm objective lens. Process parameters of 600 Hz pulse repetition frequency

and 60 mW average power where established to manage recast and glass micro-cracking. The borosilicate coverslips were also laminated with tape to manage debris deposition on the surrounding surface. The in-line pore-pore distance was *ca.* 300 μm. Following micropore array fabrication, surface silanization was performed at the ANFF-SA facilities. To selectively coat one side of the membrane and the inner walls of the pores, one side of the membrane was adhered to low tack blue tape. The exposed side was then activated with oxygen plasma (5 min, 800 mTor, Harrick plasma unit). Subsequently, the membranes and 40 μl of trichloro(1H,1H,2H,2H-perfluorooctyl)silane were placed in a sealed chamber under vacuum at 70° C for 1 h, following a previously reported method,[31] in order to effect the vapour silanization of the exposed glass surfaces. The intention here was to make one surface of the glass membrane and the inner walls of the pores hydrophobic, thus facilitating the introduction of the organic phase into the pores. Independent surface analytical measurements showed that modification took place on only one side of the membrane, but two separate batches of membranes were treated on different sides, either the laser entry or the laser exit sides, to assess the role of pore geometry. The laser entry side presented pore diameters of *ca*. 50 μm and the exit side *ca*. 25 μm, resulting in conical pores with a taper of ~6°.

Microscopic and surface characterisation. Scanning electron microscopy (SEM) images were recorded using a Tescan Mira3 FESEM. Images of the substrate coated with 3 nm Pt were taken with a beam of 5 kV, using the In Lens secondary electron detector. The determination of the pore array dimensions from the SEM images was performed using ImageJ software. X-ray photoelectron spectroscopy (XPS) was performed on glass membranes without a conductive coating using a Kratos AXIS Ultra DLD system, with monochromated Al Kα X-rays (photon energy 1486.7 eV). A coaxial hot filament electron source was used to compensate for sample charging and binding energies were then calibrated by assigning the C 1s peak to 284.5 eV. Contact angle measurements were performed with a contact angle goniometer (CAM 100, KSV Instruments, Finland). The measurements were performed in triplicate on different locations of the glass substrates after rinsing with acetone.

Electrochemical measurements. The glass membrane was glued to a glass tube (*ca.* 5.3 mm diameter) with glass silicone (Selley, Australia & New Zealand) with the hydrophobic side facing the glass cylinder so the organic solvent can be placed inside it, and consequently inside the pores, assuming that the inner walls of the pores are silanized. The silicone was allowed to cure for 24 h and the assembly was subsequently rinsed with acetone and dried in air before electrochemical experiments. The organic phase (*ca.* 150 μL) was first added to the glass tube to facilitate the filling of the pores with DCH. Following its insertion into the aqueous solution, ~200 μL of aqueous reference solution was added on top of the organic phase. Note that the liquid level should be tuned to compensate the capillary forces. Then, two Ag/AgCl electrodes together with the liquid electrolyte solutions were used to create the electrochemical cell (Scheme 1, Figure SI-1). Unless stated otherwise, electrochemical experiments were carried out using a Metrohm Autolab PGSTAT101 electrochemical analyzer and NOVA 1.9 software (Metrohm, Herisau, Switzerland). The uncompensated resistance (R_u) of the 2-electrode cell was measured, using a CHI900B potentiostat (CH Instruments Inc., USA), by positive feedback at the open circuit potential with a pulse of 50 mV amplitude. R_u values for cases A (interfaces at laser entry side) and B (interfaces at laser exit side) were 733 kOhm and 865 kOhm, respectively. All experimental voltammograms were corrected via iR compensation, *a posteiori*, using NOVA 1.9 software, which applies the formula: $E_{actual} = E_{applied} - iR_u$. In this work, transfer of a cation from aqueous to organic (or of an anion from organic to aqueous) phases was defined as a positive current.

Simulations. Simulations were performed using the finite element method (FEM) program package COMSOL Multiphysics® Ver. 3.5a. Transport was assumed to be by diffusion only. The diffusion domain approach[32] was used to reduce the three dimensional geometry to an axial symmetrical two dimensional domain. This is an adequate approximation because the number of pores in the glass membrane is high and the overall size of the array is in the millimetre range.[33] Meshes were generated from triangular

elements and free mesh parameters were used at locations of high concentration gradients. These locations are the points of the orifices at both sides of the pore and along the boundary line where both liquid phases are in contact. Here, the maximal sizes of the triangular elements were set to 0.0002 with a factor of 1.1 for element expansion. These mesh parameters have been tested previously and shown to deliver acceptable error limits (<1%) in the calculated current.[34,35] Space coordinates in the axial symmetric system were made dimensionless by dividing with the pore radius, either of the laser entry side (r_{a1}) or the laser exit side (r_{a2}), depending on the configuration of the glass membrane in the electrochemical cell. A sketch of the computational domains for both configurations is shown in Figure 1. Assuming that the pore walls are hydrophobic due to the vapour functionalisation procedure, the pores are filled with the organic phase. The shape of the liquid-liquid interface is modelled as a quarter of an ellipse, so that there is an additional parameter b, equivalent to the minor axis of an ellipse with the dimensionless pore radius (one) being equivalent to the major axis. Hence, when $b=0$ the interface is flat, when $b=-1$ the interface forms a hemisphere extending into the aqueous phase (convex form), and for $b=1$ the hemisphere extends into the pore (concave form). The maximum value of the R coordinate is calculated following the diffusion zone approach for a square lattice, $r_{max}=r_c/\pi^{1/2}$, in dimensionless form, $R_{max}=r_{max}/r_{a1}$ and r_{max}/r_{a2}. Here, r_c is the centre-to-centre separation of adjacent pores and r_{a1} and r_{a2} are the pore radii for the laser entry side (Figure 1A) and laser exit side (Figure 1B). Note that these radii are different and therefore the dimensionless values of R_{max} and the membrane thickness L, as shown in Figure 1, are different. The semi-infinite bulk boundaries are located at Z_{max} and these value are calculated from $Z_{max}=L+6(prange)/P$ and -$Z_{max}= -6(prange)^{1/2}/P$,[36,37] where L is the dimensionless pore depth (equivalent to the dimensionless membrane thickness, $P=(r_{ai} |z| F v /(RTD))^{1/2}$ ($i=1, 2$) is a dimensionless sweep rate parameter,[38] with v the sweep rate and D the diffusion coefficient of the transferring ion of charge z, and $prange$ is the dimensionless potential range, $2(E_{switch}-E_{start})RT/(|z|F)$.

The kinetics of ion transfer across the ITIES is treated as a quasi-reversible, first-order process with the potential dependence of the rate constants following a Butler–Volmer-type equation.[39-41] Thus, the Butler–Volmer equation, together with the equation of interfacial flux conservation, constitutes the boundary conditions at the interface. For more details, see reference 34.
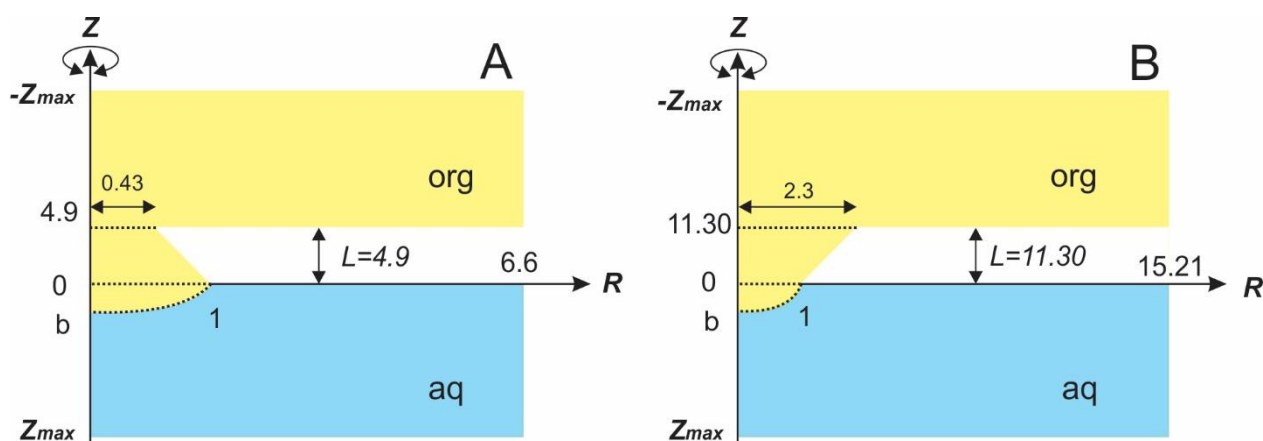

Figure 1. Sketch of the axial symmetrical computational domain (half single micro-pore) in the cases where the ITIES is located at **A** the laser entry, and **B** the laser exit configuration of the membrane. The aqueous and organic phases are denoted by aq and org, respectively. The parameter *b* controls the sphericity of the interface.

RESULTS AND DISCUSSION

Microscopic and spectroscopic characterisation

100 pores were drilled by laser ablation in the centre of a circular borosilicate glass membrane of 13 mm diameter and *ca.* 130 μm thickness. The array (10 x 10 pores) occupied a square area of approximately 2.8 x 2.8 mm and was in a square geometry. The size of the pores formed in the glass on the laser entry and exit sides differed by ~30 μm in diameter (Figure 2, left-hand side). This provides a characteristic conical shape to the pores, as has been reported previously for laser-ablated pores in thin membranes.[16,42] SEM images of the arrays were obtained to determine the pore diameters, the pore-to-pore distances and the roughness of the edges of the pores. From those images (Figure 2), the centre-to-centre distance and the

pore diameters were determined (Table 1). The laser-entry side of the pores had diameters of 53 ± 3 µm (Figure 2a-c), while the laser exit side of the pores had diameters of 23 ± 1 µm (Figure 2d-f), resulting in conical pores with a taper of ~6°.

Figure 2a shows the laser entry side of the 100 micropores. Figures 2b and 2c show magnifications of 16 pores and a single pore, respectively, which is the wider (laser entry) side of the conical pore. Similar SEM images are shown in Figure 2d-f for the laser exit side (smaller openings) of the substrate. In Figure 2e-f, a significant corona-like structure is shown to be present on the laser exit side of glass. This effect is attributed to re-solidified glass debris from the drilling process. Similar features have been reported and attempts to minimise this effect have been taken by drilling in a sandwich manner with a liquid layer between two thin glass membranes.[42]
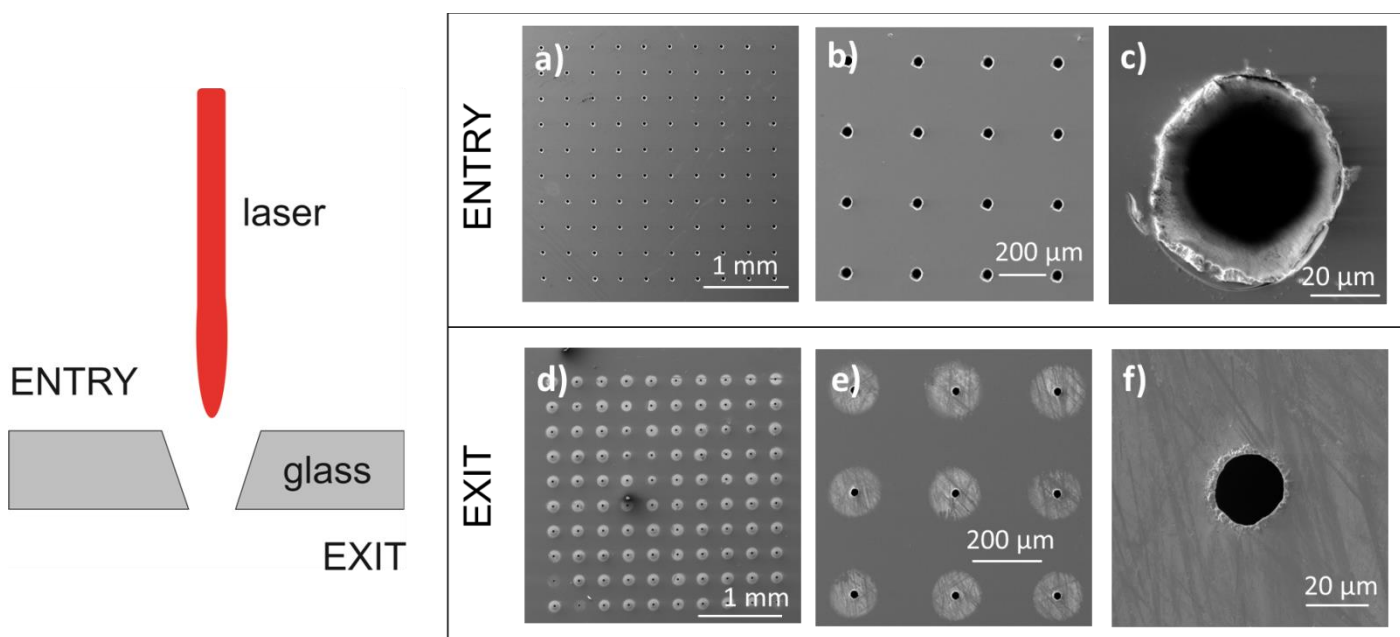

Figure 2. Scheme of the laser entry and exit in the glass substrate (left hand side) along with SEM images of the pores at the laser entry side (a to c) and the laser exit side (d to f).

Table 1. Dimensions of the micropore arrays determined from SEM imaging.

	Distance / µm	Standard Deviation (n = 9) / µm
Linear centre-to-centre (r_c)	310	±4

Diagonal centre-to-centre	437	±2
Entry side pore diameter (r_{a1})	53	±3
Exit side pore diameter (r_{a2})	23	±1

Cross-sectional images were also taken of a randomly broken glass membrane (Figure 3). Figure 3a-c illustrates the conical shape of the micropores. In Figure 3a the laser exit pore mouths can also be visualised. Close-up images of the inner walls of two different pores are shown in Figures 3b and 3c, which show very porous walls in comparison to the intact glass. This is attributed to changes of temperature in the drilling zone which promotes the solidification of the molten glass within the inner side of the hole, creating the porous walls. In Figure 3d, the SEM image of a single micropore (exit side, 11.5 µm radius) shows the roughness of the pore edges, as result of debris deposition around the pore mouth. Also, the patterned lines/cracks across the conical pores (Figures 3e and f) are a result of the milling process, such as the application of sequential short laser pulses and the use of the trepanning optic.
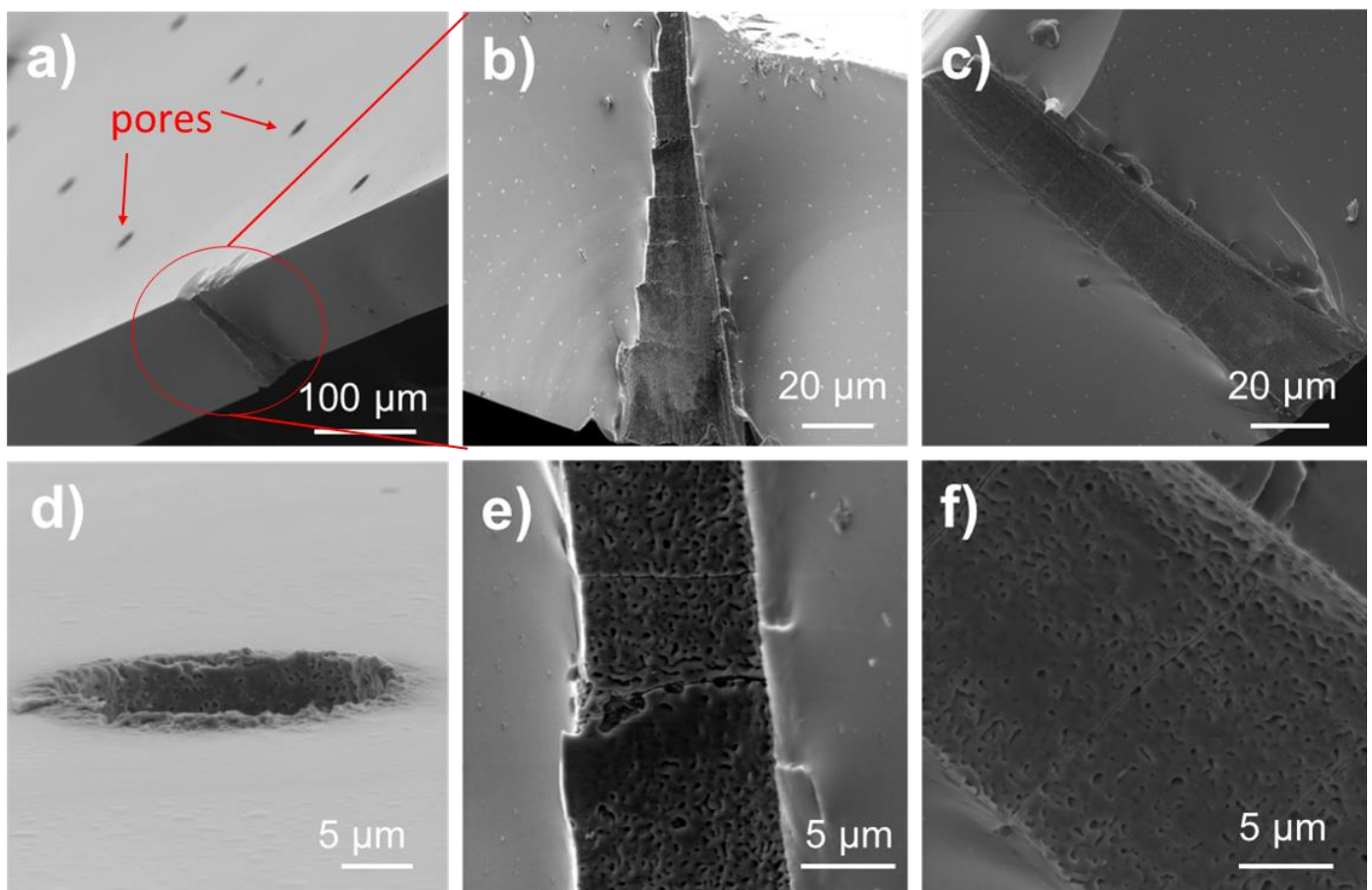
Figure 3. SEM image of a-c) cross-section of the glass substrate, d) edge of a micro-pore laser exit side and e-f) amplification of the inner wall of a micro-pore.

The drilled membranes were vapour-coated with a hydrophobic silane (trichloro(1H,1H,2H,2H-perfluorooctyl)silane) on one side, in order to render the glass surface and the pore walls hydrophobic. To characterise the glass substrate after this coating, water contact angle (CA) measurements were carried out on each side of the membranes. The CA for the modified surface (glass with the fluorinated silane) was 107 ± 6°, while for the uncoated side the CA was 39 ± 2°. These data suggest an effective coating of the glass, rendering one side hydrophobic and the other side hydrophilic. However, further analyses were performed to fully characterise the modified membranes.

XPS was carried out to evaluate the chemical composition of the surfaces after vapour silanization. Figure 4 shows XPS spectra obtained for either side of such membranes after the silanization process.
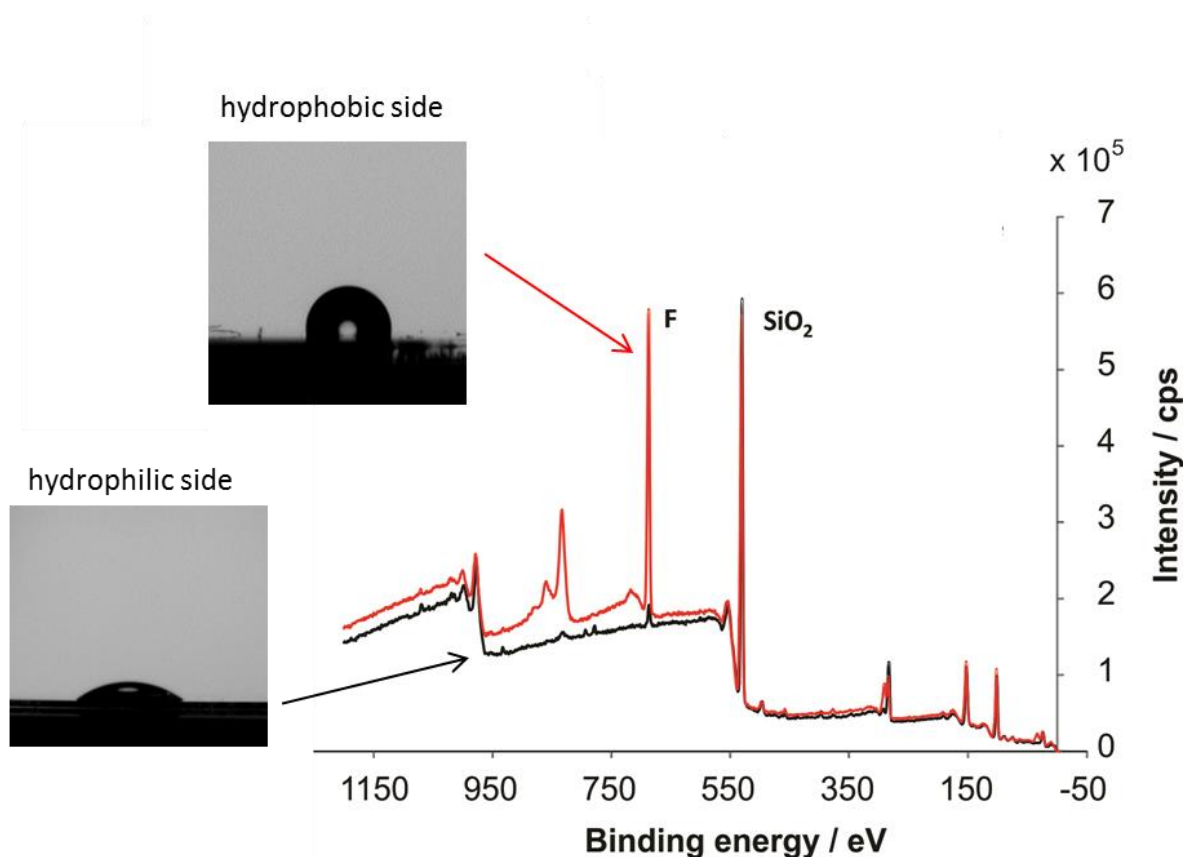
Figure 4. XPS spectra determined on either side of the coated borosilicate substrates: (—) hydrophilic side and (—) hydrophobic side. The images relate to the indicated CA measurements.

Both sides of the membrane show strong O 1s (531 eV) and Si 2p (102 eV) peaks, predominately arising from the borosilicate substrate. Further peaks from the substrate (B, Na, K and Al)[24] appear at much lower intensities, reflecting their concentration in the glass. The hydrophobic side, however, has a much more prominent F 1s signal at 687.7 eV. The absolute signal from the F 1s peak increases by a factor of just over 19 between the hydrophilic side and hydrophobic side, indicating a much greater degree of functionalisation by the fluorinated coating on the hydrophobic side. Assuming the majority of the oxygen signal arises from the substrate, the increase in F 1s signal intensity corresponds to a change in surface composition from 2.5 % fluorinated coating on the hydrophilic side to 38.8 % on the hydrophobic side. Given the XPS depth sensitivity of approximately 2-5 nm and the expected coating thickness of *ca.* 2 nm for a silane monolayer, such a percentage likely reflects full coverage on the hydrophobic side. The residual fluorine present on the hydrophilic side observed by XPS is supported by the CA values, as the hydrophilic side presents a slightly greater (<10°) CA compared to bare glass (~32°).[43]

The combination of SEM, CA and XPS measurements provided a comprehensive characterisation of the glass membrane, in terms of physical dimensions of the micropores as well as surface coatings of the glass designed to support formation of the ITIES with electrolyte phases on either side, although direct analysis of the surface coatings on the pore walls was not possible.

Electrochemical characterisation

The glass microporous membranes were employed to pattern an ITIES in a μITIES array, with organic electrolyte placed on the hydrophobic side and aqueous electrolyte on the untreated side of the membrane. Because the hydrophobic silane vapour was introduced on one side of the membrane only, it

was anticipated that the internal pore walls were also coated with the reagent. As a result of the hydrophobic functionalisation of either the laser entry side or laser exit side of the glass microporous membrane, electrochemical experiments were performed with arrays of two different diameter pores: (*i*) the hydrophobic laser exit side (Figure 5A) and (*ii*) the hydrophobic laser entry side (Figure 5B). These µITIES arrays were characterised via cyclic voltammetry (CV) of tetrapropylammonium cation (TPrA$^+$) transfer across the water – DCH interface. Additionally, micro-pore array membranes which did not undergo the silanization process were also investigated electrochemically (Figure SI-2). The large sloping current observed using micro-ITIES array formed at glass membranes without silanization is in stark contrast to the voltammogram obtained on the micro-ITIES array formed at a silanized glass membrane. These results suggest the formation of a larger unstable interface as a result of the aqueous phase filling the pores. This behaviour shows the need for the hydrophobic silane layer in order to fill the ~130 µm long micro-pores with the organic phase and enable the formation of the ITIES at the micro-pores.

The behaviour of TPrA$^+$ is well established and studied at the ITIES and can be used as a model ion for characterisation of liquid-liquid interfaces.[25,44] When the applied potential difference at the interface reaches the free energy of transfer for TPrA$^+$ ($\Delta G_{TPrA+}^{O'w \to DCH}$ = -8.3 kJ mol^{-1}),[45] the transfer of TPrA$^+$ from the aqueous phase to the organic is promoted. This process is reversed (transfer back to the aqueous) when the interfacial potential is reduced below $\Delta G_{TPrA+}^{O'w \to DCH}$. Cross-section diagrams of single cone-shaped micropores are presented in Figure 5 for the two cases studied here: the hydrophobic layer (thick dashed line) is located at the laser exit side (A) or at the laser entry side (B). For both cases, experimental and simulated CVs are presented for the 10 x 10 micro-ITIES array. Figures 5a and 5b show CVs obtained for the transfer of different concentrations of TPrA$^+$ (5 to 50 µM) across the water-DCH microinterface arrays. Figure 5c and 5d show simulated CVs for the same processes, enabling a direct comparison of the data sets. The parameters employed for the simulations are: centre-to-centre separation (r_c) 310 µm, pore depth (*L*) 130 µm, pore radius (r_a) 26.5 µm (Figure 4c) or 11.5 µm (Figure 4d), number of pores (N_p) 100,

diffusion coefficient of TPrA$^+$ in aqueous (D_{TPrA+}^{w}) 6.2 x 10^{-6} cm^2 s^{-1},[46,47] ion charge (z) +1 and sweep rate (v) 5 mV s^{-1}. Identical diffusion coefficients in the aqueous and organic phase were assumed. Figure SI-3 (Supporting Information) shows the overlapped voltammograms (simulation and experimental) for 50 μM TPrA$^+$.

The experimental results show good agreement with the simulated data across the concentration range studied. The experimental CVs obtained for the transfer of TPrA$^+$ at the wider μITIES (Figure 5a) show a steady-state current on the forward scan and a peak-shaped reverse current at 0.25 V, as reported previously for micro-ITIES located at pore mouths.[34] Furthermore, it was observed that the forward currents are lower when the liquid-liquid micro-interfaces are formed on the laser exit side (Figure 5b and d) than on the laser entry side (Figure 5a and c), as expected due to the difference in the interfacial area. It can also be noted that the reverse peak is more pronounced when the interface is formed at the laser entry side (Figure 5a) than the exit side (Figure 5b) and this is supported by the simulation data (Figure 5c and d). This effect is due to the different geometries of the pores, as was shown by a theoretical study on optimisation of stripping voltammetry at micro-ITIES.[35] For configuration A (Figure 5a and c), the pore walls are tapered towards the organic side of membrane so that after the analyte has crossed the interface its diffusion is hampered by the pore walls. Consequently diffusion away from the interface on the organic side is restricted, unlike the situation in configuration B where the tapering of the pore walls is in the opposite direction. Thus, the larger interfacial area (laser entry side) together with the tapered pore geometry promotes the accumulation of analyte within the pore close to the interface before its transfer back to the aqueous phase. A larger reverse peak current is obtained compared to the smaller interfaces (formed at laser entry side). Comparison of the reverse peaks of the experimental and simulated CVs for both micro-ITIES arrays shows that there is good agreement in the transfer peak potential of TPrA$^+$ from DCH to the aqueous phase (Figure 5). Without use of iR compensation, there is a shift in experimental

versus simulated peak potentials (Figure SI-3), which is greater at the micro-ITIES with the larger interface area.
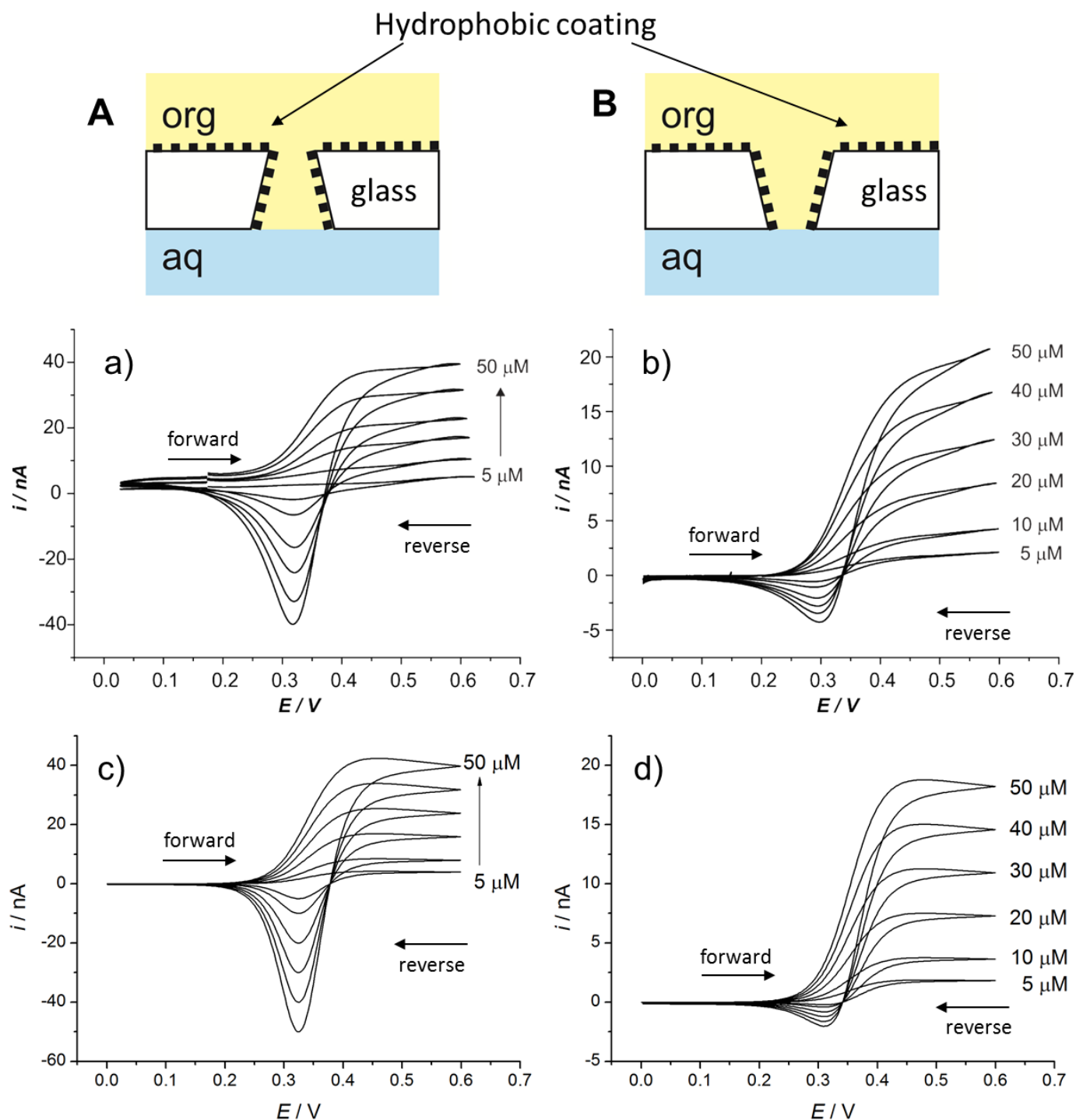

Figure 5. Sketchs (top) of cross-sections of a single cone-shaped pore where the location of the hydrophobic layer is indicated with a thick dashed line. The interface is located at the laser entry (A) or the laser exit (B) side of the membrane. The voltammograms display the corresponding experimental (a, b) and simulated (c, d) cyclic voltammograms for different concentrations of tetrapropylammonium chloride (5, 10, 20, 30, 40 and 50 µM) in 10 mM LiCl. The experimental CVs have been background-subtracted (CV of

10 mM LiCl) and iR compensated. Organic phase: 1,6-dichlorohexane. Scan rate: 5 mV s^{-1}. Note: the current-axes differ from (A), CVs a and c, to (B), CVs b and d. All CVs correspond to the full 10 x10 micro-ITIES array.

At in-laid micro-scale interfaces, in which the organic phase fills the pores, the transfer of TPrA$^+$ from aqueous to organic phase is controlled by radial diffusion, thus the diffusion zone is larger than the micro-pores. No diffusion zone overlap was observed in any of the forward scans on the time-scale of the experiments as no peak-shaped currents were observed in the forward signal. A peak shape in the forward scan would indicate linear diffusion which could be a result of overlapped diffusion layers or if the pores were filled with aqueous solution.

Using the expression formulated by Davies and Compton,[48] $\delta \approx \sqrt{2D\frac{\Delta(\Delta_o^W\varphi)}{\upsilon}}$, the diffusion zone thickness (δ) was estimated to be 250 µm at 5 mV s^{-1}, where D is the diffusion coefficient of TPrA$^+$, v is the scan rate, and $\Delta(\Delta_o^W\varphi)$ is the potential range from the onset of ion transfer current to the steady state current (0.3 V). The size of the diffusion zone is larger than the micro-pore radius ($\delta > r_a$) and half the centre-to-centre separation ($r_c/2$ = 155 µm) at 5 mV s^{-1}, so some extent of diffusion zone overlap is expected (and was seen in the simulations, Fig. 6c,d). The equi-concentration lines in the diffusion profiles (Figure SI-4) indicate a small deviation from purely spherical diffusion fields, especially for case A, which is in agreement with the prediction from Davies and Compton.

Several studies have investigated the optimum separation between micro-disks or micro-pores to avoid overlapping of the individual diffusion layers. Saito proposed that the minimum separation between electrodes must be larger than 12 times the radius of the micro-disk electrode ($r_c > 12r_a$)[49] for purely radial diffusion in a micro-disk array whilst Alfred & Oldham and Fletcher & Horne recommend $r_c > 20r_a$.[50,51] In both of experiments here, the pore-to-pore separation (r_c) is constant (r_c = 310 µm) but the radii of the pores differ (r_a = 26.5 or 11.5 µm). The ratio pore-to-pore separation / pore radius (r_c/r_a) of the glass membranes is *ca.* 12 and 27, both of which fulfil Saito's relation whilst only the side of the membrane

exposing the smaller micropores (11.5 μm, laser exit side) meets the recommendation of Alfred & Oldham and Fletcher & Horne. These data are a clear example of the difficulty to use a simple universal relationship between r_c and r_a in order to discern diffusion overlapping in micro-pore arrays. It is clear that the diffusion coefficient of the analyte, scan rate (time-scale of the experiment) and the pore radius are crucial in a good evaluation of the diffusion zone and therefore the shielding (overlapping) effect.

Interface location

To evaluate the location of the liquid-liquid interface at the microporous glass membrane, four models which depended on the format of the ITIES were used to analyse the experimental data: 1) in-laid disc interface, 2) hemispherical interface, 3) cylinder-recessed interface, and 4) cone-recessed interface.[52] The first three models are adapted from the analogous microdisc electrode behaviours[49,53-55] and the fourth one was reported by Lanyon et al.[52] for nanopore array electrodes. These correspond to the following equations (*Eq. 1 -4*);

$$i_{\lim} = 4\,|\,z\,|\,FDCr_a \qquad\qquad \text{in-laid disc} \qquad\qquad (1)$$

$$i_{\lim} = 2\pi\,|\,z\,|\,FDCr_a \qquad\qquad \text{hemispherical} \qquad\qquad (2)$$

$$i_{\lim} = \frac{4\,|\,z\,|\,FDCr_a^2}{4L + \pi r_a} \qquad\qquad \text{cylinder-recessed disc} \qquad\qquad (3)$$

$$i_{\lim} = \frac{4\,|\,z\,|\,FDCr_O r_L}{4L + \pi r_O} \qquad\qquad \text{cone-recessed disc} \qquad\qquad (4)$$

where i_{lim} is the steady-state current (A), z the charge of the ions, F the Faraday constant (C mol^{-1}), D the diffusion coefficient (cm^2 s^{-1}), C the concentration (mol cm^{-3}) of the ions in bulk aqueous solution (as we are dealing with radial diffusion from the aqueous to the interface), L the length of the interface recess within the pore, r_a the radius of the pore, and r_o and r_L are the small radius and the larger radius in a conical pore, respectively. Both L and r are expressed in cm.

For this analysis, the previously-stated parameters for the simulations were used with these equations, and interfaces formed on either side of the glass membranes were investigated. In Figure 6A, a radius of 26.5 µm was employed (laser entry side of glass) in the calculations and compared to the experimental forward currents. Similarly, a radius of 11.5 µm (laser exit side) was used in Figure 6B. The currents for the smaller interface appear to fit best to the case of an array of hemispherical interfaces (Figure 6B). The SEM images for the pore mouths (Figure 2,d-f, Figure 3d) revealed that the mouth of the pores were surrounded by an extended corona formed from debris in the fabrication step. This, combined with the silanisation, could favour formation of the hemispherical geometry. However, the larger interfaces (Figure 6A) did not follow this behaviour, although this might be due to greater difficulty in accurate measurements (see standard deviations in Table 2) around the pore surface, as the pores presented deep cracks and deformations around the laser entry area. Nevertheless, interfaces formed on the laser entry side were consistent with inlaid discs, while those on the laser entry side were consistent with hemispheres.
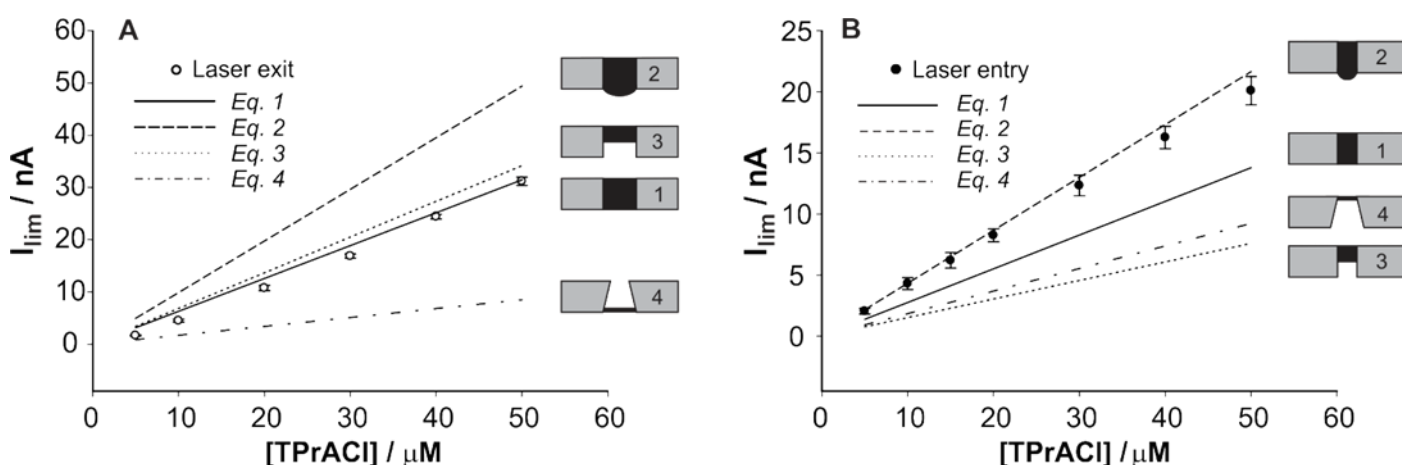

Figure 6. A) Limiting current measured at the micro-interfaces formed at the laser entry (○) and B) at the laser exit (●) sides and the calculated currents for 1) in-laid (—), 2) hemispherical (- - -), 3) 50 % recessed (···) and 4) 100% conical-recessed (-··-) interfaces with (A) pore radius of 26.5 µm and (B) pore radius of 11.5 µm. The numbers in the pore sketches refer to the equation numbers in the text. The current values correspond to the full 10 x 10 micro-ITIES arrays.

Computer simulations allow investigation of more variations than the analytical expressions, Equations (1)-(4). Therefore, for a better assessment of the electrochemical signal, additional simulations were carried out. For the laser exit and laser entry side configurations, simulations of the forward scan (ion transfer from the aqueous to the organic phase) were carried out, taking into account sphericity of the interface, as expressed by the parameter b described in Figure 1 and the Simulation method section. The simulated voltammograms were obtained for 40 μM TPrA$^+$ for different values of b, ranging from 0 through -0.125, -0.25 and -0.5 to -1. A direct comparison between the experimental result and the simulated curves is presented in Figure 7. The experimental data correspond to a b value of ca. -0.25 in the case of the widest interface (26.5 μm radius), and to b = -1 for the 11.5 μm radius, which corresponds to a hemispherical configuration. These results are in agreement with the analysis presented in Figure 5 where the experimental values were compared to equations (1) to (4).
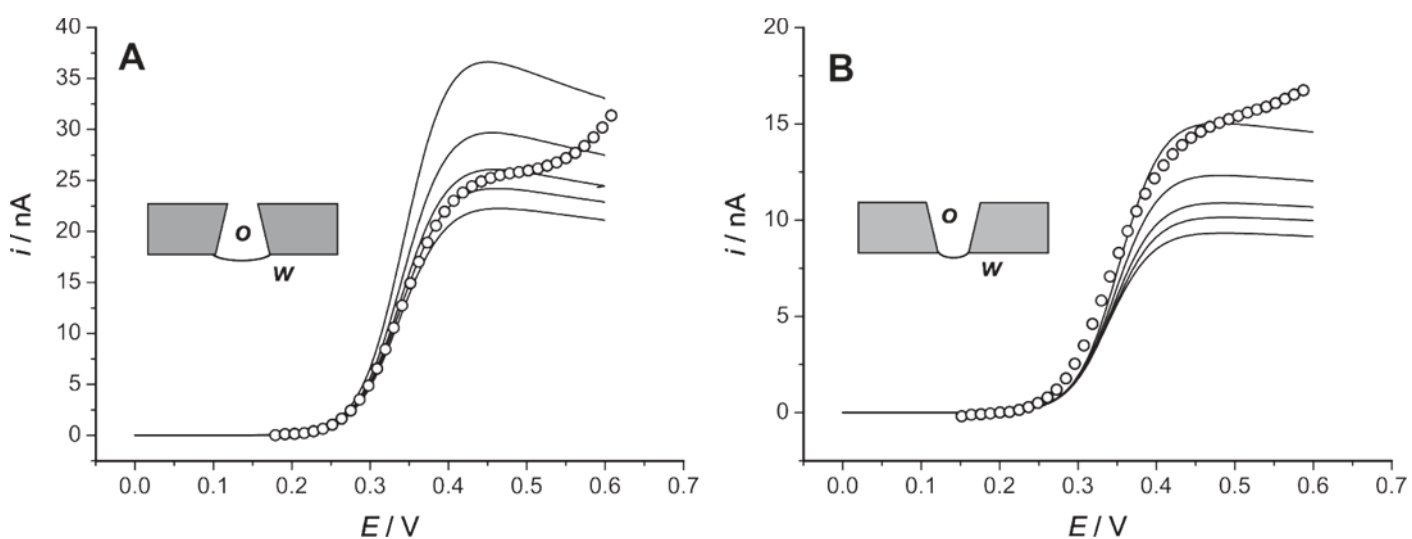

Figure 7. Simulated (lines) voltammograms of the forward scan showing the effect of sphericity parameter of the interface; b = 0 (flat), -0.125, -0.25, -0.5 and -1 (increasing currents). The symbols (○) are experimental values for the transfer of 40 μM TPrA$^+$ at interface located on (A) laser entry side and (B) laser exit side for the 10 x 10 micro-ITIES array. The experimental data were background-subtracted and iR-compensated.

These simulation results confirm the shapes and locations of the interface for the 100 hemispherical microinterface array of 11.5 µm radii. They also confirm the difficulty to determine the size and location of the interface on the larger radii side of the conical pores. The flatter interface (b = -0.25) is believed to be affected by i) the larger size of the interface, ii) the roughness and cracks at the edge of the cone, iii) less circular pores due to these edge imperfections, iv) the similar densities of the organic and water phases, and v) less pressure forces (compared to the smaller interface) induced by the organic reference solution located on top of the organic phase which deforms the interface.
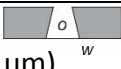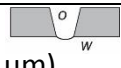
Analytical parameters

The concentration calibration curves for three separate experiments in each of the configurations investigated showed good linearity in the range between 5 and 50 µM TPrA$^+$. The standard deviation determined from the interfaces located at the laser entry side data (Table 2) suggests a larger variation in the interface locations. From the calibration curves in Figure 6, two interesting trends were observed: i) the area of the interface formed on the laser entry side is significantly larger, as the current was increased by ~10 nA for 50 µM TPrA$^+$, and ii) the coefficient of determination (R^2, Table 2) is larger for the case where the interfaces are located on the laser exit side (11.5 µm radius). This means that better overall precision is obtained when the interfaces are formed at the smaller pore mouths of the conical pores, because the stability of the water/DCH interface decreases as the interfacial area increases. Precision values for repeated experiments at fixed concentrations were also determined as shown in Table 2 (%RSD for 5 and 50 µM TPrA$^+$). DCH possesses a density of 1.07 g cm^{-3} (298 K)[56] which, combined with pressure forces, deforms the interface and resultants in greater variability at the larger interfaces. The roughness at the larger pore mouths also contributes to this viability.

The limits of detection (LOD) determined at the larger radii are 5.3 µM and 3.6 µM for the forward and reverse peaks, respectively. However, for the smaller radii, the LODs decreased to 0.8 and 1.8 µM for the

forward and reverse peaks, respectively (see Table 2). The laser exit side exhibits less variability whereas the entry side enables larger currents but is accompanied by greater variability in the voltammetric analysis and hence a larger LOD. The fact that the reverse peak at the interface located on the laser exit side is *ca*. 10 times lower than the forward current is reflected in the lower sensitivity (slope of the calibration curve) and therefore the higher LOD.

Table 2. Analytical parameters from the voltammetric measurements.

		Sweep	Sensitivity[a] / nA µM^{-1}	Intercept / nA	R^2	$S_{y/x}$ / nA	LOD[b] / µM	%RSD[c] (5 µM)	%RSD[c] (50 µM)
Entry side (radius 26.5 µm)		Forward	0.644	-2.533	0.990	1.146	5.3	0.3	23.2
		Reverse	0.702	-1.409	0.996	0.847	3.6	7.5	22.9
Exit side (radius 11.5 µm)		Forward	0.400	0.198	0.999	0.116	0.8	11.2	11.9
		Reverse	0.079	-0.073	0.999	0.0479	1.8	5.8	3.3

[a] The sensitivity is obtained for 6 concentrations of the analyte (5 to 50 µM) each measured in 3 independent experiments (n = 3).
[b] LOD was estimated based on $3S_{y/x}/m$, where $S_{y/x}$ is the standard deviation of the residuals and m is the calibration graph sensitivity.
[c] %RSD is the % relative standard deviation at a single concentration for 3 independent measurements (n = 3).

CONCLUSIONS

This work presents a laser micromachined borosilicate glass membrane as a microinterface array holder for electrochemical detection at liquid-liquid interfaces. The laser ablation strategy produces conical pores with a taper of *ca*. 6º in glass coverslips of 130 µm thickness, in a 10x10 square array format. The glass micropore arrays were selectively silanized to enable interface location at either laser entry or laser exit side of the membrane. The pore radii were 11.5 µm (laser exit side) or 26.5 µm (laser entry side), while the pore centre-to-centre separation (r_c) was 310 µm and was found to be sufficient to avoid diffusion zone overlap on either side of the membrane when analysing tetrapropylammonium transfer at 5 mV s^{-1}. Voltammetric ion transfer across water-DCH microinterface arrays was used to characterise the membranes in conjunction with finite element simulations. A lower variability was seen in the voltammetry of interfaces located at the laser exit side, which improved the sensitivity of the system in comparison to

the laser entry side of the membrane. The computational simulations suggested a hemispherical interface was formed on the laser exit side. These membranes provide a platform for the formation of liquid-liquid microinterface arrays as a basis for electrochemical sensing.

Supporting Information

Images of membranes and electrochemical cell set-up, and the composition of the electrochemical cell; Comparison of CVs with membranes without and with hydrophobic treatment; Comparison in overlaid format of experimental and simulated CVs; Concentration contour lines around micro-pores obtained from the simulation study.

REFERENCES

(1) Girault, H. H. *Electroanalytical Chemistry, A Series of Advances vol. 23*, Bard, A. J.; Zoski, C. G., Eds.; CRC Press, 2010, 1-104.
(2) Arrigan, D. W. M.; Herzog, G.; Scanlon, M. D.; Strutwolf, J. In *Electroanalytical Chemistry, A Series of Advances vol. 25*, Bard, A. J.; Zoski, C. G., Eds.; CRC Press, 2013, pp 105-178.
(3) Herzog, G. *Analyst* **2015**, *140*, 3888-3896.
(4) Samec, Z. *Pure Appl. Chem.* **2004**, *76*, 2147-2180.
(5) Liu, S. J.; Li, Q.; Shao, Y. H. *Chem. Soc. Rev.* **2011**, *40*, 2236-2253.
(6) Taylor, G.; Girault, H. H. J. *J. Electroanal. Chem.* **1986**, *208*, 179-183.

(7) Liu, S. J.; Dong, Y. T.; Zhao, W. B.; Xie, X.; Ji, T. R.; Yin, X. H.; Liu, Y.; Liang, Z. W.; Momotenko, D.; Liang, D. H.; Girault, H. H.; Shao, Y. H. *Anal. Chem.* **2012**, *84*, 5565-5573.

(8) Stockmann, T. J.; Montgomery, A. M.; Ding, Z. F. *J. Electroanal. Chem.* **2012**, *684*, 6-12.

(9) Wang, Y.; Kececi, K.; Velmurugan, J.; Mirkin, M. V. *Chem Sci* **2013**, *4*, 3606-3616.

(10) Shen, M.; Ishimatsu, R.; Kim, J.; Amemiya, S. *J. Am. Chem. Soc.* **2012**, *134*, 9856-9859.

(11) Shao, Y. H.; Liu, B.; Mirkin, M. V. *J. Am. Chem. Soc.* **1998**, *120*, 12700-12701.

(12) Chen, C.-C.; Zhou, Y.; Baker, L. A. *Annu. Rev. Anal. Chem.* **2012**, *5*, 207-228.

(13) Wang, Y. X.; Kakiuchi, T.; Yasui, Y.; Mirkin, M. V. *J. Am. Chem. Soc.* **2010**, *132*, 16945-16952.

(14) Wang, Y.; Velmurugan, J.; Mirkin, M. V.; Rodgers, P. J.; Kim, J.; Amemiya, S. *Anal. Chem.* **2010**, *82*, 77-83.

(15) Li, Q.; Xie, S.; Liang, Z.; Meng, X.; Liu, S.; Girault, H. H.; Shao, Y. *Angewandte Chemie International Edition* **2009**, *48*, 8010-8013.

(16) Campbell, J. A.; Girault, H. H. *J. Electroanal. Chem.* **1989**, *266*, 465-469.

(17) Wilke, S.; Osborne, M. D.; Girault, H. H. *J. Electroanal. Chem.* **1997**, *436*, 53-64.

(18) Wilke, S.; Zerihun, T. *Electrochim. Acta* **1998**, *44*, 15-22.

(19) Peulon, S.; Guillou, V.; L'Her, M. *J. Electroanal. Chem.* **2001**, *514*, 94-102.

(20) Mastouri, A.; Peulon, S.; Farcage, D.; Bellakhal, N.; Chaussé, A. *Electrochim. Acta* **2014**, *120*, 212-218.

(21) Faisal, S. N.; Pereira, C. M.; Rho, S.; Lee, H. J. *Phys. Chem. Chem. Phys.* **2010**, *12*, 15184-15189.

(22) Lee, H. J.; Beattie, P. D.; Seddon, B. J.; Osborne, M. D.; Girault, H. H. *J. Electroanal. Chem.* **1997**, *440*, 73-82.

(23) Hossain, M. M.; Girault, H. H.; Lee, H. J. *Bull. Korean Chem. Soc.* **2012**, *33*, 1734-1740.

(24) Hossain, M. M.; Faisal, S. N.; Kim, C. S.; Cha, H. J.; Nam, S. C.; Lee, H. J. *Electrochem. Commun.* **2011**, *13*, 611-614.

(25) Liu, Y.; Sairi, M.; Neusser, G.; Kranz, C.; Arrigan, D. W. M. *Anal. Chem.* **2015**, *87*, 5486-5490.

(26) Peulon, S. *Electrochim. Acta* **2009**, *54*, 1537-1544.

(27) Zazpe, R.; Hibert, C.; O'Brien, J.; Lanyon, Y. H.; Arrigan, D. W. M. *Lab Chip* **2007**, *7*, 1732-1737.

(28) Scanlon, M. D.; Strutwolf, J.; Blake, A.; Iacopino, D.; Quinn, A. J.; Arrigan, D. W. M. *Anal. Chem.* **2010**, *82*, 6115-6123.

(29) Rimboud, M.; Hart, R. D.; Becker, T.; Arrigan, D. W. M. *Analyst* **2011**, *136*, 4674-4681.

(30) Sairi, M.; Chen-Tan, N.; Neusser, G.; Kranz, C.; Arrigan, D. W. M. *ChemElectroChem* **2015**, *2*, 98-105.

(31) Gilles, S. *Chemical Modification of Silicon Surfaces for the Application in Soft Lithography*; Forschungszentrum, Zentralbibliothek, 2007.

(32) Gueshi, T.; Tokuda, K.; Matsuda, H. *J. Electroanal. Chem. Interfacial Electrochem.* **1978**, *89*, 247-260.

(33) Sliusarenko, O.; Oleinick, A.; Svir, I.; Amatore, C. *Electroanalysis* **2015**, *27*, 980-991.

(34) Strutwolf, J.; Scanlon, M. D.; Arrigan, D. W. M. *Analyst* **2009**, *134*, 148-158.

(35) Strutwolf, J.; Arrigan, D. W. M. *Anal. Bioanal. Chem.* **2010**, *398*, 1625-1631.

(36) Britz, D. *Digital Simulation in Electrochemistry*, 3rd ed.; Springer-Verlag: Berlin Heidelberg, 2005.

(37) Britz, D.; Strutwolf, J. *Digital Simulation in Electrochemistry*, 4th ed.; Springer-Verlag: Berlin Heidelberg, in preparation.

(38) Heinze, J. *Berichte der Bunsengesellschaft für physikalische Chemie* **1981**, *85*, 1096-1103.

(39) Girault, H. H. J.; Schiffrin, D. J. *J. Electroanal. Chem. Interfacial Electrochem.* **1985**, *195*, 213-227.

(40) Samec, Z. *J. Electroanal. Chem. Interfacial Electrochem.* **1979**, *99*, 197-205.

(41) Strutwolf, J.; Manzanares, J. A.; Williams, D. E. *Electrochem. Commun.* **1999**, *1*, 139-144.

(42) Yu, M.; Kim, H. S.; Blick, R. H. *Opt. Express* **2009**, *17*, 10044-10049.

(43) Sumner, A. L.; Menke, E. J.; Dubowski, Y.; Newberg, J. T.; Penner, R. M.; Hemminger, J. C.; Wingen, L. M.; Brauers, T.; Finlayson-Pitts, B. J. *Phys. Chem. Chem. Phys.* **2004**, *6*, 604-613.

(44) Sairi, M.; Strutwolf, J.; Mitchell, R. A.; Silvester, D. S.; Arrigan, D. W. M. *Electrochim. Acta* **2013**, *101*, 177-185.

(45) Katano, H.; Senda, M. *Anal. Sci.* **2001**, *17*, 1027-1029.

(46) Li, X.; Shantz, D. F. *The Journal of Physical Chemistry C* **2010**, *114*, 8449-8458.

(47) Lide, D. R.; CRC Press, Boca Raton, FL, 2005, p 2660.

(48) Davies, T. J.; Compton, R. G. *J. Electroanal. Chem.* **2005**, *585*, 63-82.

(49) Saito, Y. *Rev. Polarogr.* **1968**, 177 - 187.

(50) Alfred, L. C. R.; Oldham, K. B. *J. Electroanal. Chem.* **1995**, *396*, 257-263.

(51) Fletcher, S.; Horne, M. D. *Electrochem. Commun.* **1999**, *1*, 502-512.

(52) Lanyon, Y. H.; De Marzi, G.; Watson, Y. E.; Quinn, A. J.; Gleeson, J. P.; Redmond, G.; Arrigan, D. W. M. *Anal. Chem.* **2007**, *79*, 3048-3055.

(53) Bond, A. M.; Luscombe, D.; Oldham, K. B.; Zoski, C. G. *J. Electroanal. Chem.* **1988**, *249*, 1-14.

(54) Arrigan, D. W. M. *Analyst* **2004**, *129*, 1157-1165.

(55) Penner, R. M.; Heben, M. J.; Longin, T. L.; Lewis, N. S. *Science* **1990**, *250*, 1118-1121.
(56) Yaws, C. L. *Thermophysical Properties of Chemicals and Hydrocarbons* **2008**, 1-809.

TOC Graphic: